Microsc. Microanal. 18, 711–719, 2012
doi:10.1017/S1431927612000499

Microscopy AND Microanalysis

On-Column 2*p* Bound State with Topological Charge ±1 Excited by an Atomic-Size Vortex Beam in an Aberration-Corrected Scanning Transmission Electron Microscope

Huolin L. Xin* and Haimei Zheng

Materials Sciences Division, Lawrence Berkeley National Laboratory, Berkeley, CA 94720, USA

Abstract: Atomic-size vortex beams have great potential in probing the magnetic moment of materials at atomic scales. However, the limited depth of field of vortex beams constrains the probing depth in which the helical phase front is preserved. On the other hand, electron channeling in crystals can counteract beam divergence and extend the vortex beam without disrupting its topological charge. Specifically, in this article, we report that atomic vortex beams with topological charge ±1 can be coupled to the 2*p* columnar bound states and propagate for more than 50 nm without being dispersed and losing its helical phase front. We give numerical solutions to the 2*p* columnar orbitals and tabulate the characteristic size of the 2*p* states of two typical elements, Co and Dy, for various incident beam energies and various atomic densities. The tabulated numbers allow estimates of the optimal convergence angle for maximal coupling to 2*p* columnar orbital. We have also developed analytic formulae for beam energy, convergence angle, and hologram-dependent scaling for various characteristic sizes. These length scales are useful for the design of pitch-fork apertures and operations of microscopes in the vortex-beam imaging mode.

Key words: electron vortex beam, aberration-corrected electron microscopy, topological charge, electron channeling, columnar orbital

Introduction

Recently, the ability to create an electron beam that carries specified orbital angular momentum (Uchida & Tonomura, 2010; Verbeeck et al., 2010, 2011*b*; Bliokh et al., 2011; Herring, 2011; Idrobo & Pennycook, 2011; McMorran et al., 2011*a*, 2011*b*; Schattschneider & Verbeeck, 2011) has generated immense interest for its potential to measure the magnetic moment of 3*d* and rare earth elements at atomic scales (Schattschneider, 2008; Xin & Muller, 2010*a*; Schattschneider et al., 2012). Mathematically, the complex wave function that contains an orbital angular momentum of $l\hbar$ can be written as $\Psi = e^{il\varphi}f(r)$, where φ is the azimuthal angle, r is the radial coordinate, and l is the topological charge. Vortex beams are defined as such beams with nonzero topological charges and with the wave amplitude going to zeros at $r = 0$ giving a phase singularity in the center (Nye & Berry, 1974; Bazhenov et al., 1990; Allen et al., 1992). Optical vortex beams have been studied intensively (Heckenberg et al., 1992; Beirjersbergen et al., 1994; Basistiy et al., 1995; He et al., 1995; Brand, 1999; O'Neil et al., 2002; Padgett et al., 2004) and have found numerous applications in a wide range of fields such as optical tweezing (Curtis et al., 2002; Grier, 2003) and quantum optics (Kapale & Dowling, 2005). In a similar manner to optical vortex beams, in an electron microscope, high-energy electrons that carry orbital angular momentums can be generated either using a helical phase plate (Uchida & Tonomura, 2010) or a computer-generated hologram (Verbeeck et al., 2010; McMorran et al., 2011*b*). The electron vortex beam has become more promising; as shown theoretically by Xin and Muller (Xin & Muller, 2010*a*) and later by Schattschneider, Verbeeck and their coworkers experimentally (Verbeeck et al., 2011*a*; Schattschneider et al., 2012), subnanometer or even atomic-size beams with topological charge ±1 can be formed if the probe forming aperture at the prespecimen focal plane is replaced by a pitchfork hologram aperture. With the simplicity to create micron-scale features on metal foils using current lithography and focused ion beam technology, this concept can be realized in most modern instruments. Optical and electron vortex beams are in many ways similar both in their wave nature and their generation optics (Bliokh et al., 2007). However, there are fundamental differences between them (Henderson, 1995). Apart from absorption, light and X rays weakly interact with solids allowing the kinematic theory of light propagation to hold. Therefore, not much attention has been paid to study how multiple elastic scattering can modify the chirality of a vortex beam in the optical and X-ray community. Electrons, however, are strongly elastically scattered in materials. The strong elastic interaction with solids, also known as channeling in on-axis crystals (Kirkland et al., 1987; Loane et al., 1988; Hillyard et al., 1993; Hillyard & Silcox, 1993), immediately raises alert that the desired chirality of the vortex beam may vanish or change even in very thin specimens. Thus, this requires scrutiny of vortex beam propagation in crystals. In this work we show that an electron vortex beam with a carefully chosen convergence angle can efficiently couple to

Received December 27, 2011; accepted March 30, 2012
**Corresponding author*. E-mail: hxin@lbl.gov

the on-column $2p$ state ($l = 1$) that carries the same topological charge. The helical phase front of the incident vortex beam can be preserved while channeling on column. On the other hand, when propagating in vacuum, the helical phase is only preserved while the beam is within the depth of field.

The propagation of high-energy electrons in an ideal crystal is described by Bethe's Bloch-wave dynamical theory (Bethe, 1928; Hirsch et al., 1965; Allen et al., 2003). To solve the problem rigorously, all the reflections in the reciprocal lattice need to be considered. However, the Ewald sphere of high-energy electrons is relatively flat. Therefore, including only the reflections in the First Order Laue Zone in the calculation is a proper first order approximation (Pennycook & Jesson, 1990; Nellist & Pennycook, 1999; Geuens & Van Dyck, 2002). Translating this into real space language, it means an on-crystal can be approximated by a two-dimensional (2D) array of rods. Each rod is described by an average attractive potential, as screened by the core and valence electrons. Each rod of screened charges can support cylindrical bound states on them in a similar manner to the atomic orbitals around atoms (Geuens & Van Dyck, 2002; Anstis et al., 2003; Van Aert et al., 2007). A tight-binding calculation can recover the dispersion relations (Hovden et al., 2010). However, if the overlap of states from neighbor columns are sufficiently small, as are the deep core orbitals of atoms in solids, the dispersion surface is nearly flat and columnar states can be considered to be isolated or well-defined (Pennycook & Jesson, 1990; Van Dyck & deBeeck, 1996; Anstis et al., 2003). These well-defined columnar states carrying their specified orbital angular momentum (or topological charge) can be selectively excited by an incident beam that has the same angular momentum. For example, an ideal convergent beam when positioned on-column can only couple to the s states for its cylindrical symmetry. However, with the creation of on-column atomic-size vortex beams, columnar states with nonzero topological charges can be excited selectively. This selectivity allows the chirality of the incident vortex beam to be preserved on-column. As the $2p$ state has zero amplitude at $r = 0$, it is a natural vortex state that is supported in a crystal. Therefore, it does not only preserve the topological charge but also preserves the vortex nature. The crystal columns serve as a depth-of-focus extender that counteracts the divergence nature of a convergent beam.

To provide a full picture of atomic-size vortex beam and its elastic interaction with a crystal, the remainder of the article is organized as follows. First, we will review how an atomic-size vortex beam can be created in an electron microscope and give the scalings of various characteristic dimensions of vortex beams as a function of the convergence angle. Second, we will review the scattering theory and lay down the radial Schrodinger equation needed for solving the columnar states. Third, we will show how the vortex beam can be coupled to the $2p$ state and channel on the column without losing its vortex nature.

Atomic-Size Vortex Beam and Its Free Propagation

It has been shown that the Fourier transform of a pitchfork aperture can produce vortex beams with topological charge ± 1 in the first side bands of the central beam (Bazhenov et al., 1990; Allen et al., 1992). In a transmission electron microscope (Verbeeck et al., 2010; McMorran et al., 2011*b*), this has been experimentally verified by diffracting off the aperture in the image plane. However, as shown by Idrobo and Pennycook (2011), it is impractical to create subnanometer vortex beams using this approach. However, the Fourier transform can be carried out in reverse. By placing the pitchfork aperture in the back focal plane of the probe forming lens, atomic-size vortex beams are formed at the front focal plane (Fig. 1a) (Xin & Muller, 2010*a*). Figure 1b shows an example of the amplitude and phase of the central convergent beam and the first two side bands. As clearly indicated by the phase map shown in Figure 1b, the two side beams have a helical phase front: the phase increases by 2π as it goes around the vortex core.

Figure 2 shows the peak radius (R_{peak}), the Rayleigh radius (R_{Rayleigh}), and the full-width at half-maximum (FWHM) of the vortex beam with a topological charge of one as a function of the convergence angle.[a] (Here following the Rayleigh criterion, the Rayleigh radius is defined as the distance from the center to the first minimum of the side lobe.) These are various dimensions defined to characterize the size of the vortex beam. The same as the scaling for any convergent beam, the dimension of the beam is proportional to the wavelength of the incident electron and is inversely proportional to the convergent angle. The prefactor differs in different measurements of the beam size. For example, the prefactor for the Rayleigh radius is 0.91. It is 50% larger than the more familiar factor—0.61—for a convergent beam formed by a round aperture.

The phase around the vortex core is perfectly helical when the beam is at its optimal defocus. However, due to the divergence nature of a convergent beam, the helical phase front can be destroyed. To illustrate this effect, Figure 3 shows the propagation of the wave front away from the perfect defocus plane. We find that first the amplitude part of the vortex beam diverges in size as the beam propagates. Second, the phase part of the vortex beam becomes a spiral pattern. Third, the interferences from the central beam can strongly modify the side bands as the beam propagates further. At 20 nm, we can see that the helical nature of the side beam is completely destroyed by the interferences coming from the divergent central beam. The depth at which such strong interference occurs can be estimated by $(N/2)(\lambda/\alpha_{\text{max}}^2)$, where the λ is the wavelength of the incident electron, α_{max} is the convergence semiangle, and N is the number of "white" streaks in the pitchfork

[a]In the remaining text, convergence angle is the same as convergence semiangle unless otherwise specified.

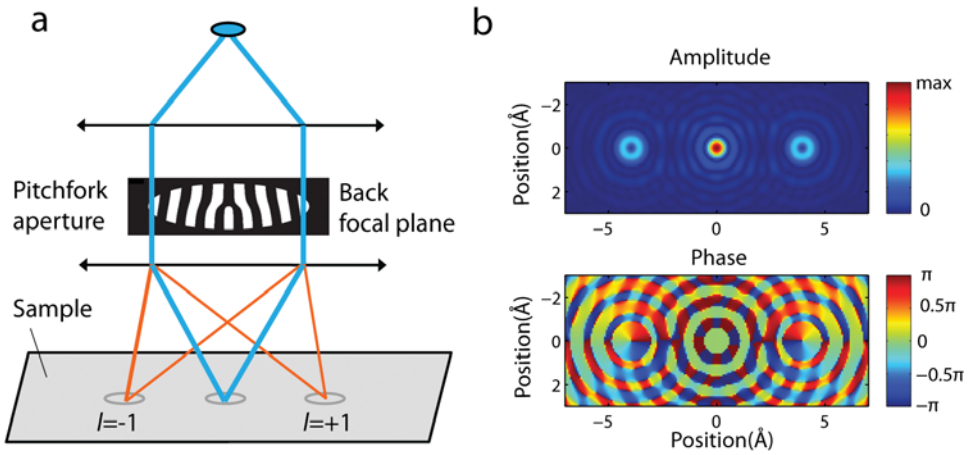

Figure 1. The formation of atomic-size vortex beams with topological charge one. **a:** The optical schematic. **b:** The amplitude and the phase of the central and the vortex side bands at the optimal defocus (300 keV, $\alpha_{max} = 20$ mrad). The pitchfork hologram aperture was generated by threshholding the interference pattern generated by coherent superposition of a helical phase front and a plane wave. We chose the same number of fringes as used in Verbeeck et al. (2010).

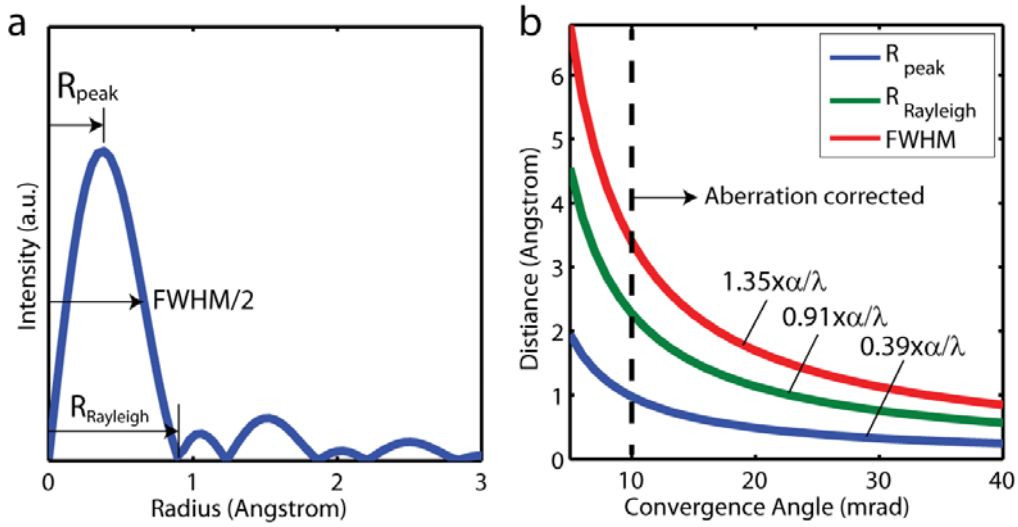

Figure 2. Scaling of the sizes of a vortex beam as a function of wavelength and convergence semiangle. **a:** The radial amplitude of a vortex beam with topological charge one (300 keV, $\alpha_{max} = 20$ mrad). **b:** Various characteristic dimensions as a function of the convergence semiangle.

aperture (for instance, $N = 8$ in Fig. 1). [One would notice this is $N/4$ times the depth of focus $2\lambda/\alpha_{max}^2$ of a convergent electron beam (Intaraprasonk et al., 2008; Xin & Muller, 2009, 2010*b*).] Therefore, given a chosen thickness and the convergence angle, the number of fringes needed in the aperture to ensure that the vortex side bands are not strongly influenced by the central beam can be calculated by $N = d/(\lambda/\alpha_{max}^2)$. ($d$ is the thickness. We assume the beam is focused at the center of the sample in depth.) The results for four typical beam voltages are tabulated in Figure 4. It provides a guideline for designing pitchfork apertures.

Propagation in Crystals

In the last section, we have studied the propagation of a vortex beam in vacuum. It was shown that the vortex beam diverges as it propagates away from the optimal focal plane. However, this phenomenon can be significantly modified by electron channeling. In this section, we will first develop the theory for solving the columnar bound states on atomic columns that are responsible for electron channeling. Then we will show that coupling to the $2p$ bound state helps prevent the vortex beam from diverging as it propagates on-column.

The Scalar Relativistic-Corrected Schrodinger Equation

The speed of a 300 keV electron is 0.78 times the speed of light. Strictly speaking, the elastic scattering of such electrons should be solved with the Dirac equation. However, it has been shown by Rujiwara, Hashimoto and more recently by Rother and Scheerschmidt that a scalar-relativistic-corrected Schrodinger equation is accurate enough for 300-keV electrons (Fujiwara, 1961; Hashimoto, 1964; Rother &

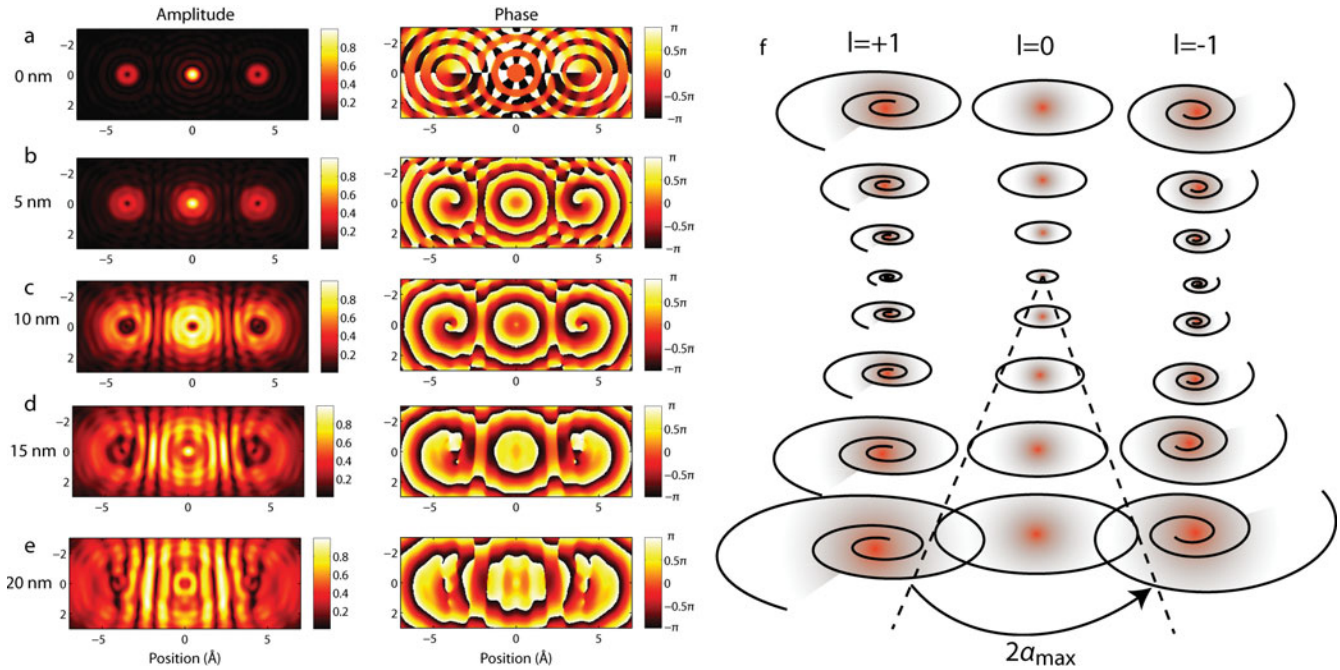

Figure 3. The free propagation of the vortex beams (300 keV, $\alpha_{max} = 20$ mrad) in vacuum. The amplitude and phase of the wave function at (**a**) 0 nm, (**b**) 5 nm, (**c**) 10 nm, (**d**) 15 nm, and (**e**) 20 nm away from the optimal focal plane. (**f**) The schematics of the free propagation of vortex beams.

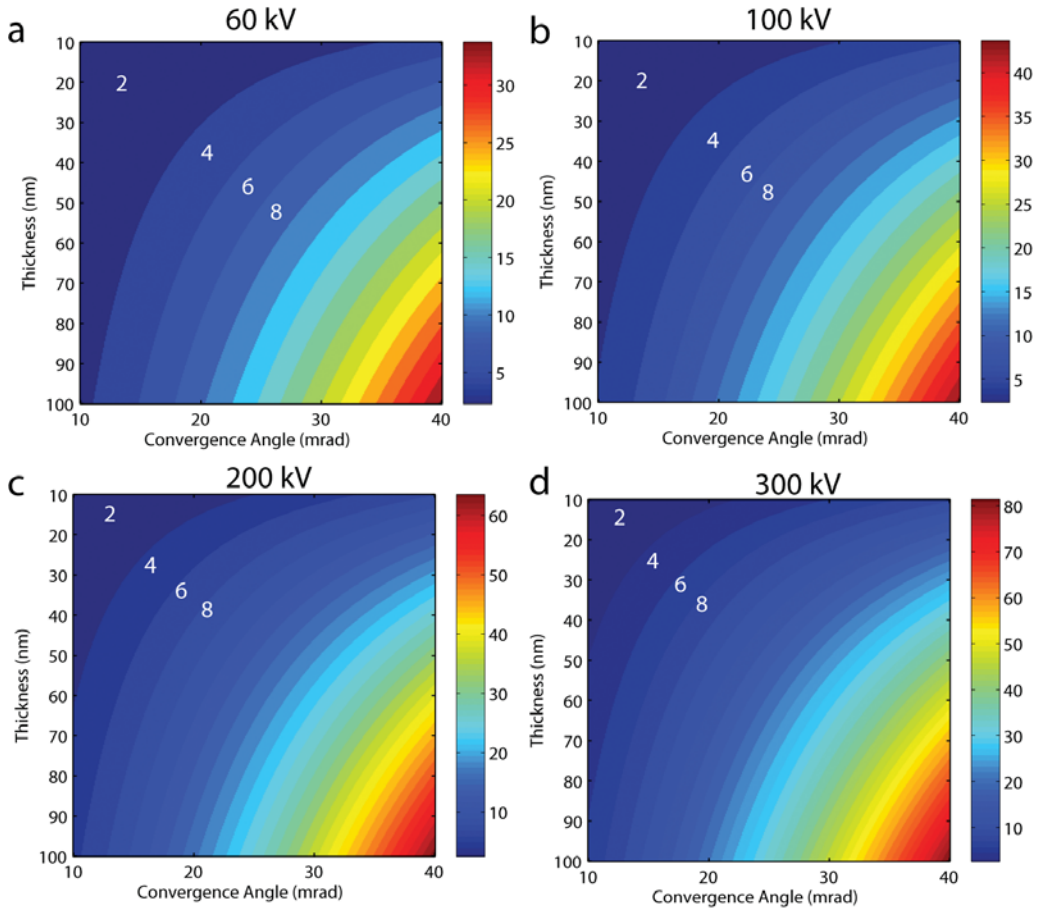

Figure 4. The least number of fringes required to minimize interference from the central beam as the vortex beam propagates. The plots show the calculations for (**a**) 60 keV, (**b**) 100 keV, (**c**) 200 keV, and (**d**) 300 keV.

Scheerschmidt, 2009). In addition, for high-energy electrons, the exchange and correlation with the electrons in the solids can be neglected (Wu & Ohmura, 1962; Mott & Massey, 1965). Therefore, the elastic scattering of an electron can be described by a Schrodinger equation for the atomic potential (the Coulomb potential of the nuclei as screened by the innershell and valence electrons) (Cowley & Moodie, 1957; Fujiwara, 1961; Humphreys, 1979; Gratias & Portier, 1983):

$$\left[-\frac{\hbar^2}{2m}\nabla^2 - eV(r)\right]\Psi(r) = E\Psi(r), \tag{1}$$

where $m = \gamma m_0$ is the relativistic mass, $-e$ is the charge of an electron, V is the screened atomic potential inside the sample, and E is the incident kinetic energy of the electron.

To solve forward propagation of high-energy electrons in *real space* governed by Equation (1), we need to make two approximations. The first one is to assume the wave function $\Psi(x, y, z)$ can be written as a product of two factors—one fast varying term along z, $\exp(2\pi iz/\lambda)$, and one slow-varying envelope term $\psi(x, y, z)$ (Cowley & Moodie, 1957; Van Dyck & Coene, 1984; Kirkland, 2010):

$$\Psi(x, y, z) = \psi(x, y, z)\exp\left(\frac{2\pi iz}{\lambda}\right), \tag{2}$$

where λ is the relativistic wavelength of the high-energy electron ($\lambda = h/\sqrt{2\gamma m_0 E}$). The second approximation is the forward scattering approximation (Van Dyck & Coene, 1984; Kirkland, 2010):

$$\left|\frac{\partial^2\psi}{\partial z^2}\right| \ll \left|\frac{1}{\lambda}\frac{\partial\psi}{\partial z}\right|. \tag{3}$$

The two approximations are valid because the electrons are traveling at very high speed and the deflection by a single atomic potential is relatively weak. Based on the two approximations, if we substitute equation (2) into equation (1) and drop the $\partial^2\psi/\partial z^2$ term, we have:

$$i\hbar\frac{h}{m\lambda}\frac{\partial\psi(x, y, z)}{\partial z} = \left[-\frac{\hbar^2}{2m}\nabla_{xy}^2 - eV(x, y, z)\right]\psi(x, y, z). \tag{4}$$

The propagation of high-energy electrons governed by equation (4) can be approximately solved by the multislice method (Gratias & Portier, 1983; Van Dyck & Coene, 1984; Kirkland et al., 1987; Chen & Van Dyck, 1997).

Apart from the fact that a column of atoms is z dependent, a few bound states are supported on the column (Pennycook & Jesson, 1990; Nellist & Pennycook, 1999; Anstis et al., 2003). It is a valid approximation to expand the atomic column into a Fourier series and keep only the z-independent zero-order term, i.e., the average potential of the atomic column $V(x, y) = v_{\Delta z}(x, y)/d$. This is the same as the approximation of keeping only the zero-order Laue zone in the Bloch-wave simulation (Berry & Ozoriode, 1973). The scattering to the first, second, and higher Laue zones can be added later using time-dependent perturbations (Gratias & Portier, 1983). The z-independent potential converts equation (4) into a 2D time-independent problem (Berry & Ozoriode, 1973):

$$\left[-\frac{\hbar^2}{2m}\nabla_{xy}^2 - eV(x, y)\right]\psi_i(x, y) = E_i\psi_i(x, y). \tag{5}$$

If the incident wave function at the entrance surface is $\Psi(x, y)$, then the depth evolution of the wave function is

$$\psi(x, y, z) = \Sigma_i C_i\psi_i(x, y)\exp\left(-\frac{i}{\hbar}\frac{m\lambda}{h}E_i z\right) \tag{6}$$

$$C_i = \int\Psi(x, y)\psi_i(x, y)\,dx\,dy. \tag{7}$$

In equation (7), C_i is the coupling coefficient of the incident probe ($\Psi(x, y)$) to a particular columnar orbital $\psi_i(x, y)$. When the incident probe $\Psi(x, y)$ is cylindrically symmetric, as is in a regular scanning transmisson electron microscope, and positioned on the column, the coupling coefficient is zero for any columnar states with nonzero angular momentum such as $2p$. Now, we can transfer our knowledge of solving bound orbitals of three-dimensional (3D) atoms (Cowan, 1981; Koonin & Meredith, 1998) to the problem of solving a 2D projected screened "atom."

The Radial Equation

First, for computational convenience, we use the Ry-Bohr atomic units:

$$Ry = \frac{\hbar^2}{2m_0 a_0^2} = 13.607\text{ eV}$$

$$a_0 = \frac{\hbar^2}{m_0 e^2} = 0.529\text{ Å}.$$

Then equation (5) for a single column in cylindrical coordinates reads:

$$\nabla^2\psi(r, \theta) + \gamma[E + V(r)]\psi(r, \theta) = 0, \tag{8}$$

where γ is the relativistic gamma. $V(r)$ is the potential energy of the electron in Ry and it is positive at finite distances. Because for a single column V is cylindrically symmetric, we can perform separation of variables that has the following form:

$$\psi_{nl}(r, \theta) = c_l u_{nl}(r)\exp(il\theta) = c_l\frac{R_{nl}(r)}{r^{1/2}}\exp(il\theta), \tag{9}$$

where l is the angular quantum number or the topological charge and it can be any integer from $-\infty$ to $+\infty$. The radial wave equation for $R_{nl}(r)$ is

$$\frac{d^2R_{nl}(r)}{dr^2} + \left[\gamma E + \gamma V(r) - \frac{l^2 - \frac{1}{4}}{r^2}\right]R_{nl}(r) = 0. \tag{10}$$

Except for the relativistic correction (Berry & Ozoriode, 1973) showed the same equation.

2*p* Columnar Orbital

For p-type columnar orbitals that carry topological charge one ($l = 1$), equation (10) becomes

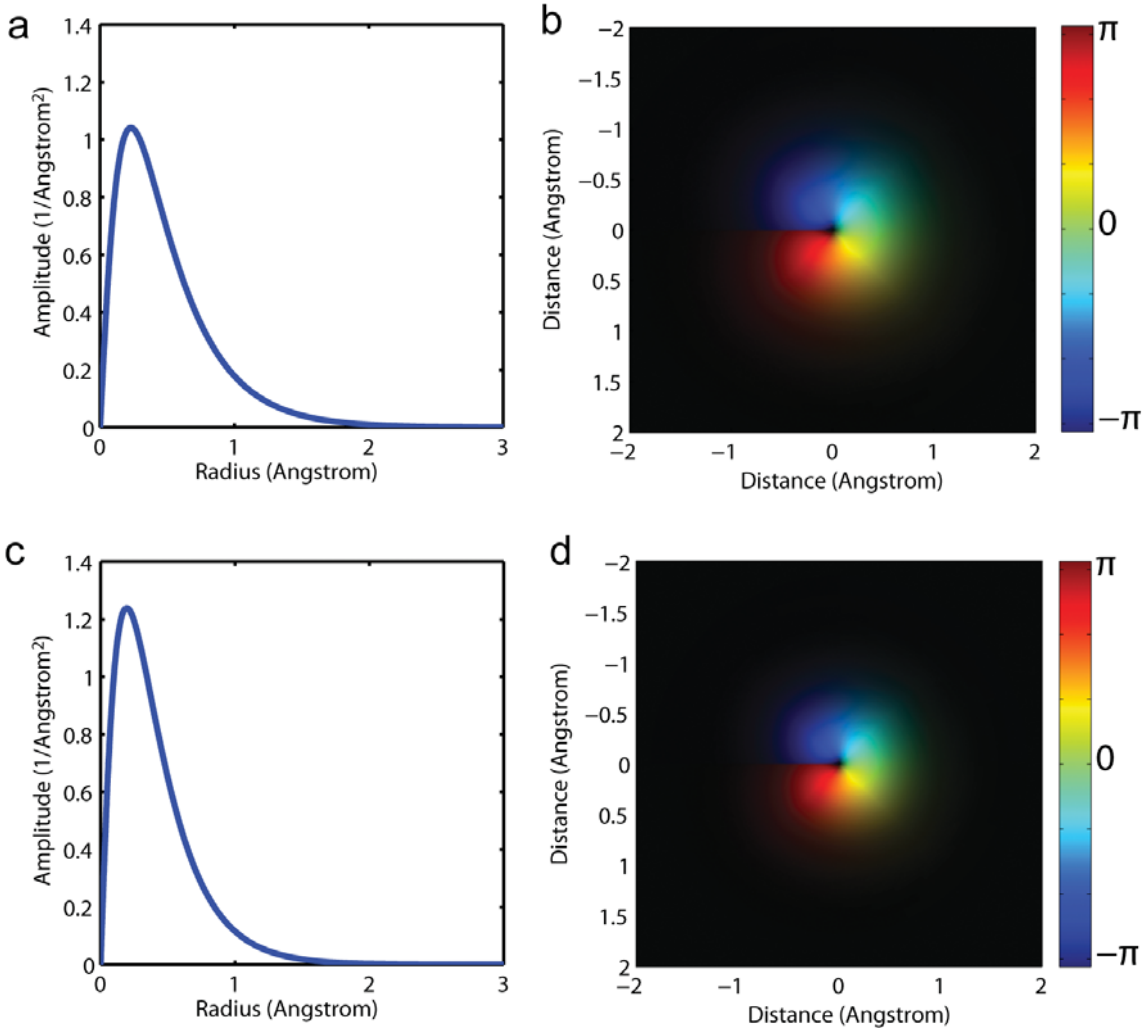

Figure 5. The 2*p* orbital with topological charge +1 of the (**a**,**b**) cobalt column with 2.5074 Å spacing (columns down hexagonal cobalt [11-20]) and the (**c**,**d**) dysprosium column with 4 Å spacing (pseudocubic perovskite [001] axis).

$$\frac{d^2R_{n1}(r)}{dr^2} + \left[\gamma E + \gamma V(r) - \frac{\frac{3}{4}}{r^2}\right] R_{n1}(r) = 0 \qquad (11)$$

It is easy to obtain the asymptotic forms of $R_{n1}(r)$:

$$R_{n1}(r) = c\exp\left[-\sqrt{\gamma|E_{n1}|}r\right] \quad \text{as } r \to \infty$$
$$R_{n1}(r) = cr^{3/2} \quad \text{as } r \to 0. \qquad (12)$$

As $u_{nl}(r) = cr \to 0$ as $r \to 0$, the amplitude of the *p* columnar orbitals is zero in the center of the orbital. Therefore, they are on-column vortex beams hosted by the crystal with topological charge one.

As we know the initial conditions from the asymptotic forms, the radial function R_{n1} can be calculated by numerical integration. A very primitive method in solving such an eigenenergy problem is the shooting method: the eigenstates can be identified when the radial function does not blow up at large distances. An improved method is to both integrate forward from $r = 0$ and integrate backward from $r = \infty$. The eigenstate can be identified when the first derivative at the connection point is continuous. The numerical integration of this second-order differential equation can be performed by a Runge-Kutta method. However, similar to solving 3D atomic orbitals, the more efficient Numerov method can be applied (Cowan, 1981; Koonin & Meredith, 1998).

Figure 5 shows the numerical solutions for two typical columns that can be found in 3*d* transition metals and in perovskite materials. Take cobalt for example, the 2*p* columnar state is plotted in Figure 5b. It is clearly a vortex beam with topological charge +1. The FWHM is only 1.22 Å. In the lateral dimension, the nearest column is positioned 2.2 Å away. This gives an overlap integral smaller than 1%, which means the 2*p* columnar orbital can be considered isolated without interference from the neighbors. If you compare the 2*p* orbital on the Co column with the 300 kV vortex beam created by an aberration-corrected electron microscopy, the size matches well. This means that for the on-column 2*p* orbital of a given material and a given zone axis, the convergence angle can be optimized such that the size of the vortex beam matches that of the 2*p* columnar orbital to maximize excitation. Figure 6 gives such guide-

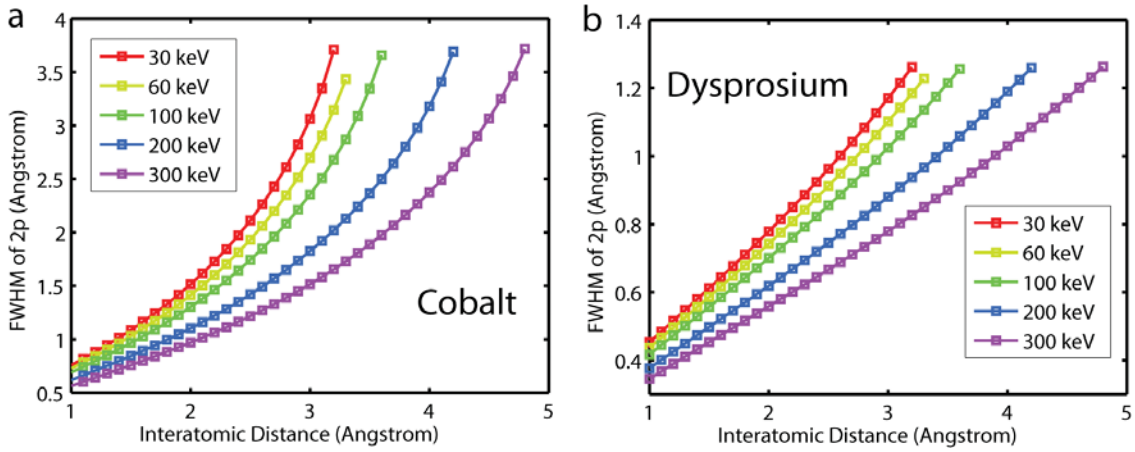

Figure 6. The FWHM of the 2*p* orbital hosted on (**a**) cobalt and (**b**) dysprosium columns at a function of the interatomic distance along the vertical column at a few typical incident beam energies. This serves as a guideline for the choice of the convergence angle for the vortex beam to maximize coupling to 2*p*.

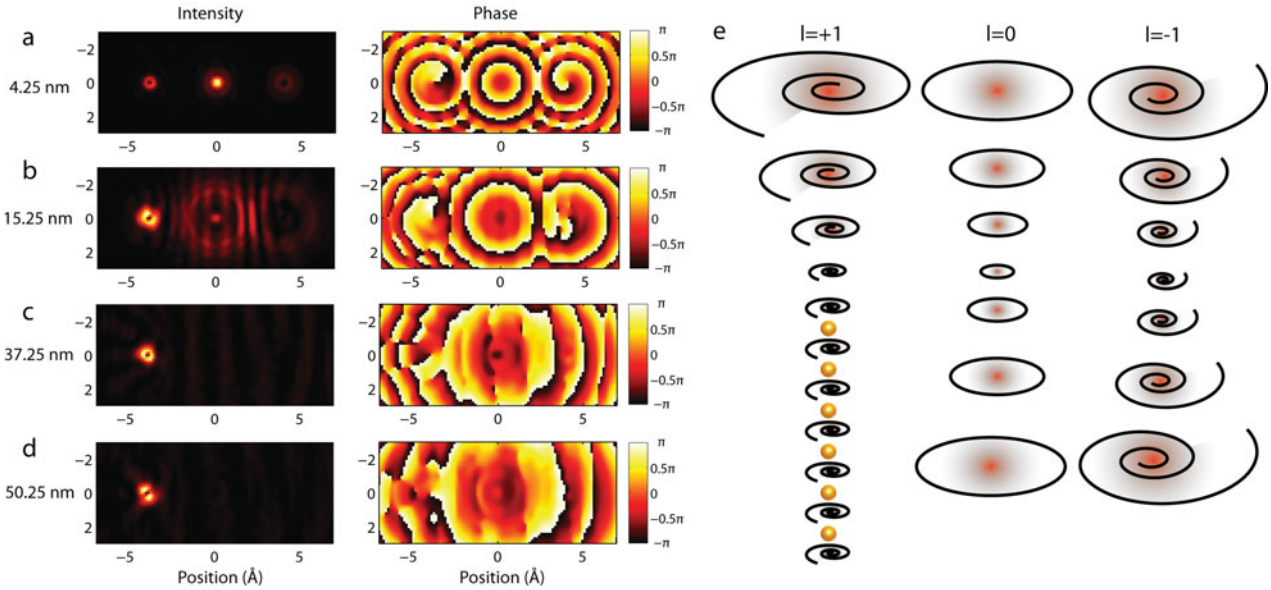

Figure 7. The multislice simulation of the propagation of the central beam and the vortex side bands with a cobalt column (2.5074 Å spacing, the column down hexagonal cobalt [11-20]) positioned in the center of the left vortex beam. The intensity and the phase of the wave function as it propagates (**a**) 4.25 nm, (**b**) 15.25 nm, (**c**) 37.25 nm, and (**d**) 50.25 nm along the column. (**e**) The schematics of the propagation of the vortex beams. The simulation was carried out by a custom-written Matlab script.

lines for two typical elements in 3*d* and rare earth. One can look up the FWHM of the 2*p* orbitals in this plot and use the equation in Figure 2 to estimate the optimal convergence angle for maximal coupling.

On-Column Channeling of Vortex Beams

Figure 7 shows the propagation of the central beam with the vortex side bands with a column of cobalt placed in the core of the left vortex. In Figures 7a and 7b, we can see the left vortex channels along the column whereas the central and right beams diverge as they propagate. The 2*p* state propagates along the column and the topological charge is preserved even at a thickness of 50 nm as shown in the phase map.

2*p* columnar orbitals can also be excited when a round beam is placed off the column. However, compared to the excitation of 1*s*, only a minimal fraction is coupled to the *p*-type bound states due to the phase symmetry. We want to note that such strong and selective excitation of 2*p* columnar orbitals is only possible with an incident beam that possesses the same orbital angular momentum.

Discussions

Even though we focused the discussion on 2*p* columnar states, the vortex beam of topological charge one can excite higher *p* states. However, the isolated column model for higher *p* states does not hold as well as it does for 2*p* orbitals

because they are more delocalized. Even for $2p$ columnar orbital, the isolated model can break down when the crystal is oriented to low-symmetry zone axis or light-element crystals are used. To apply the single column model, one needs to calculate the FWHM of the p orbital and make sure that it is smaller than the smallest column-to-column spacing in the lateral dimension. Nevertheless, as we have shown in Figure 5, in two typical materials made of $3d$ and rare earth elements oriented along high-symmetry zone axis, the high atomic density along the column attracts the $2p$ columnar orbital tight enough such that the overlap with the neighbor orbitals is ignorable. In general, high-symmetry zone axis is preferred as the lateral column-to-column spacing is high and the interatomic distance along the column is low.

As shown by McMorran et al. (2011*b*), electron vortex beams with high quanta of orbital angular momentum can be intensively generated using holograms of high-quanta helical phase fronts. This makes it possible to selectively excite columnar orbitals with absolute topological charge larger than one. However, one has to check if such orbitals are supported on the columns and if the isolated column approximation is valid.

In this article, we assume the optics are aberration free. This assumption is approximately correct in an aberration-corrected instrument with moderately chosen numerical aperture. However, in an uncorrected microscope, a modeling with the third-order spherical aberration is needed. In addition to the geometric aberrations, chromatic aberration can cause defocus blur to the beams. This effect can be important in instruments with large C_c and large energy spread (Intaraprasonk et al., 2008).

Conclusion

In this article, we first reviewed the formation of an atomic vortex beam in an aberration-corrected scanning transmission electron microscope. We presented the theoretical scalings for various characteristic sizes, including peak-intensity radius, the FWHM, and the Rayleigh radius, of the vortex beam with topological charge one. We also showed that the vortex side band diverges as well as the central beam as they propagate away from the optimal focal plane. The helical phase front can be destroyed when the central beam interferes with the side vortex bands. We developed a simple formula to calculate the least number of fringes needed in the pitchfork aperture for the distance that the vortex beam can travel without strong interferences from the central beam. Then we reviewed the theory for calculating the bound states on single atomic columns. We gave numerical solutions to the $2p$ columnar orbitals and we tabulated the FWHM of the $2p$ states of two typical elements, one $3d$ transition and one rare earth, of various incident beam energies and various interatomic distances along the column. The tabulated numbers can help to estimate the optimal convergence angle for maximal coupling to $2p$. Finally, we showed the vortex beam can channel on atomic columns and preserve the topological charge of the incident beam by coupling to the $2p$ columnar orbital with the same angular momentum. This shows that the vortex nature of a vortex beam can be extended and the beam divergence can be counteracted by an atomic column.

Acknowledgments

This work was supported by Materials Sciences Division, Lawrence Berkeley National Laboratory. H.L.X. thanks his thesis advisor David A. Muller for giving the project and countless advice on calculating columnar orbitals for electron channeling during his PhD study. H.L.X. thanks Judy J. Cha and Earl J. Kirkland for initial code and notes for solving the radial Schrödinger equation. H.L.X. also thanks Robert Hovden for helping debug the program and developing the concept of columnar orbitals.

References

Allen, L., Beijersbergen, M., Spreeuw, R. & Woerdman, J. (1992). Orbital angular momentum of light and the transformation of Laguerre-Gaussian laser modes. *Phys Rev A* **45**, 8185–8189.

Allen, L.J., Findlay, S.D., Oxley, M.P. & Rossouw, C.J. (2003). Lattice-resolution contrast from a focused coherent electron probe. Part I. *Ultramicroscopy* **96**, 47–63.

Anstis, G.R., Cai, D.Q. & Cockayne, D.J.H. (2003). Limitations on the s-state approach to the interpretation of sub-angstrom resolution electron microscope images and microanalysis. *Ultramicroscopy* **94**, 309–327.

Basistiy, I.V., Soskin, M.S. & Vasnetsov, M.V. (1995). Optical wavefront dislocations and their properties. *Opt Comm* **119**, 604–612.

Bazhenov, V.Y., Vasnetsov, M.V. & Soskin, M.S. (1990). Laser beams with screw dislocations in their wavefronts. *JETP Lett* **52**, 429–431.

Beirjersbergen, M.W., Coerwinkel, R.P.C., Kristensen, M. & Woerdman, J.P. (1994). Helical-wavefront laser beams produced with a spiral phaseplate. *Opt Comm* **112**, 321–327.

Berry, M.V. & Ozoriode, A.M. (1973). Semiclassical approximation of radial equation with 2-dimensional potentials. *J Phys A-Math Gen* **6**, 1451–1460.

Bethe, H. (1928). Theory on the diffraction of electrons in crystals. *Ann Phys* **87**, 55–129.

Bliokh, K., Bliokh, Y., Savel'ev, S. & Nori, F. (2007). Semiclassical dynamics of electron wave packet states with phase vortices. *Phys Rev Lett* **99**, 190404.

Bliokh, K.Y., Dennis, M.R. & Nori, F. (2011). Relativistic electron vortex beams: Angular momentum and spin-orbit interaction. *Phys Rev Lett* **107**, 174802.

Brand, G.F. (1999). Phase singularities in beams. *Am J Phys* **67**, 55.

Chen, J.H. & Van Dyck, D. (1997). Accurate multislice theory for elastic electron scattering in transmission electron microscopy. *Ultramicroscopy* **70**, 29–44.

Cowan, R.D. (1981). *The Theory of Atomic Structure and Spectra*. Berkeley, CA: University of California Press.

Cowley, J.M. & Moodie, A. (1957). The scattering of electrons by atoms and crystals. I. A new theoretical approach. *Acta Crystallogr* **10**, 609–619.

Curtis, J.E., Koss, B.A. & Grier, D.G. (2002). Dynamic holographic optical tweezers. *Opt Comm* **207**, 169–175.

Fujiwara, K. (1961). Relativistic dynamical theory of electron diffraction. *J Phys Soc Jpn* **16**, 2226–2238.

Geuens, P. & Van Dyck, D. (2002). The S-state model: A work horse for HRTEM. *Ultramicroscopy* **93**, 179–198.

Gratias, D. & Portier, R. (1983). Time-like perturbation method in high-energy electron diffraction. *Acta Crystallogr A* **39**, 576–584.

Grier, D.G. (2003). A revolution in optical manipulation. *Nature* **424**, 910.

Hashimoto, H. (1964). Energy dependence of extinction distance and transmissive power for electron waves in crystals. *J Appl Phys* **35**, 277.

He, H., Friese, M.E.J., Heckenberg, N.R. & Rubinsztein-Dunlop, H. (1995). Direct observation of transfer of angular momentum to absorptive particles from a laser beam with a phase singularity. *Phys Rev Lett* **75**, 826–829.

Heckenberg, N.R., McDuff, R., Smith, C.P. & White, A.G. (1992). Generation of optical phase singularities by computer-generated holograms. *Opt Lett* **17**, 221–223.

Henderson, R. (1995). The potential and limitations of neutrons, electrons and X-rays for atomic resolution microscopy of unstained biological molecules. *Q Rev Biophys* **28**, 171–193.

Herring, R.A. (2011). A new twist for electron beams. *Science* **331**, 155.

Hillyard, S., Loane, R.F. & Silcox, J. (1993). Annular dark-field imaging: Resolution and thickness effects. *Ultramicroscopy* **49**, 14–25.

Hillyard, S. & Silcox, J. (1993). Thickness effects in ADF STEM zone-axis images. *Ultramicroscopy* **52**, 325–334.

Hirsch, P.B., Howie, A., Nicholson, R.B., Pashley, D.W. & Whelan, M. (1965). *Electron Microscopy of Thin Crystals*. London: Butterworths.

Hovden, R., Xin, H.L. & Muller, D.A. (2010). Determining resolution in an abberration-corrected era: Why your probe is larger than you thought. *Microsc Microanal* **16**, 152–153.

Humphreys, C. (1979). The scattering of fast electrons by crystals. *Rep Prog Phys* **42**, 1825–1887.

Idrobo, J.C. & Pennycook, S.J. (2011). Vortex beams for atomic resolution dichroism. *J Elec Microsc* **60**, 295–300.

Intaraprasonk, V., Xin, H.L. & Muller, D.A. (2008). Analytic derivation of optimal imaging conditions for incoherent imaging in aberration-corrected electron microscopes. *Ultramicroscopy* **108**, 1454–1466.

Kapale, K.T. & Dowling, J.P. (2005). Vortex phase qubit: Generating arbitrary, counterrotating, coherent superpositions in bose-einstein condensates via optical angular momentum beams. *Phys Rev Lett* **95**, 173601.

Kirkland, E.J. (2010). *Advanced Computing in Electron Microscopy*. New York: Springer Verlag.

Kirkland, E.J., Loane, R.F. & Silcox, J. (1987). Simulation of annular dark field stem images using a modified multislice method. *Ultramicroscopy* **23**, 77–96.

Koonin, S.E. & Meredith, D.C. (1998). *Computational Physics: Fortran Version*. Boulder, CO: Westview Press.

Loane, R.F., Kirkland, E.J. & Silcox, J. (1988). Visibility of single heavy atoms on thin crystalline silicon in simulated annular dark field. *Acta Crystallogr A* **44**, 912–927.

McMorran, B., Agrawal, A., Anderson, I.M., Herzing, A.A., Lezec, H., McClelland, J.J. & Unguris, J. (2011*a*). Electron Laguerre-Gaussian beams. Conference paper. Quantum Electronics and Laser Science Conference, Baltimore, MD, May 1, 2011.

McMorran, B.J., Agrawal, A., Anderson, I.M., Herzing, A.A., Lezec, H.J., McClelland, J.J. & Unguris, J. (2011*b*). Electron vortex beams with high quanta of orbital angular momentum. *Science* **331**, 192–195.

Mott, N. & Massey, H. (1965). *The Theory of Atomic Collisions*. Oxford, UK: Clarendon Press.

Nellist, P.D. & Pennycook, S.J. (1999). Incoherent imaging using dynamically scattered coherent electrons. *Ultramicroscopy* **78**, 111–124.

Nye, J.F. & Berry, M.V. (1974). Dislocations in wave trains. *P Roy Soc A-Math Phy* **336**, 165–190.

O'Neil, A., MacVicar, I., Allen, L. & Padgett, M. (2002). Intrinsic and extrinsic nature of the orbital angular momentum of a light beam. *Phys Rev Lett* **88**, 053601.

Padgett, M., Courtial, J. & Allen, L. (2004). Light's orbital angular momentum. *Phys Today* **57**(5), 35–40.

Pennycook, S.J. & Jesson, D.E. (1990). High-resolution incoherent imaging of crystals. *Phys Rev Lett* **64**, 938–941.

Rother, A. & Scheerschmidt, K. (2009). Relativistic effects in elastic scattering of electrons in TEM. *Ultramicroscopy* **109**, 154–160.

Schattschneider, P. (2008). Exchange of angular momentum in EMCD experiments. *Ultramicroscopy* **109**, 91–95.

Schattschneider, P., Stöger-Pollach, M., Löffler, S., Steiger-Thirsfeld, A., Hell, J. & Verbeeck, J. (2012). Sub-nanometer free electrons with topological charge. *Ultramicroscopy* **115**, 21–25.

Schattschneider, P. & Verbeeck, J. (2011). Theory of free electron vortices. *Ultramicroscopy* **111**, 1461–1468.

Uchida, M. & Tonomura, A. (2010). Generation of electron beams carrying orbital angular momentum. *Nature* **464**, 737–739.

Van Aert, S., Geuens, P., Van Dyck, D., Kisielowski, C. & Jinschek, J. (2007). Electron channelling based crystallography. *Ultramicroscopy* **107**, 551–558.

Van Dyck, D. & Coene, W. (1984). The real space method for dynamical electron diffraction calculations in high resolution electron microscopy: I. Principles of the method. *Ultramicroscopy* **15**, 29–40.

Van Dyck, D. & deBeeck, M.O. (1996). A simple intuitive theory for electron diffraction. *Ultramicroscopy* **64**, 99–107.

Verbeeck, J., Schattschneider, P., Lazar, S., Stoger-Pollach, M., Loffler, S., Steiger-Thirsfeld, A. & Van Tendeloo, G. (2011*a*). Atomic scale electron vortices for nanoresearch. *Appl Phys Lett* **99**, 203109–203111.

Verbeeck, J., Tian, H. & Béché, A. (2011*b*). A new way of producing electron vortex probes for STEM. *Ultramicroscopy* **113**, 83–87.

Verbeeck, J., Tian, H. & Schattschneider, P. (2010). Production and application of electron vortex beams. *Nature* **467**, 301–304.

Wu, T.Y. & Ohmura, T. (1962). *Quantum Theory of Scattering*. New York: Prentice-Hall.

Xin, H.L. & Muller, D.A. (2009). Aberration-corrected ADF-STEM depth sectioning and prospects for reliable 3D imaging in S/TEM. *J Elec Microsc* **58**, 157–165.

Xin, H.L. & Muller, D.A. (2010*a*). Electron microscopy: A new spin on electron beams. *Nature Nanotechnol* **5**, 764–765.

Xin, H.L. & Muller, D.A. (2010*b*). Three-dimensional imaging in aberration-corrected electron microscopes. *Microsc Microanal* **16**, 445–455.